





Ultrasound characterization of the viscoelastic properties of additively manufactured photopolymer materials

Max Gattin,¹ Nicolas Bochud,^{1,a)}  Giuseppe Rosi,¹  Quentin Grossman,² Davide Ruffoni,² 
and Salah Naili¹ 

¹Univ Paris Est Creteil, Univ Gustave Eiffel, CNRS, UMR 8208, MSME, F-94010 Créteil, France

²Mechanics of Biological and Bioinspired Materials Laboratory, Department of Aerospace and Mechanical Engineering, University of Liège, Quartier Polytech 1, Allée de la Découverte 9, B-4000 Liège, Belgium

ABSTRACT:

Photopolymer-based additive manufacturing has received increasing attention in the field of acoustics over the past decade, specifically towards the design of tissue-mimicking phantoms and passive components for ultrasound imaging and therapy. While these applications rely on an accurate characterization of the longitudinal bulk properties of the materials, emerging applications involving periodic micro-architected media also require the knowledge of the transverse bulk properties to achieve the desired acoustic behavior. However, a robust knowledge of these properties is still lacking for such attenuating materials. Here, we report on the longitudinal and transverse bulk properties, i.e., frequency-dependent phase velocities and attenuations, of photopolymer materials, which were characterized in the MHz regime using a double through-transmission method in oblique incidence. Samples were fabricated using two different printing technologies (stereolithography and polyjet) to assess the impact of two important factors of the manufacturing process: curing and material mixing. Overall, the experimentally observed dispersion and attenuation could be satisfactorily modeled using a power law attenuation to identify a reduced number of intrinsic ultrasound parameters. As a result, these parameters, and especially those reflecting transverse bulk properties, were shown to be very sensitive to slight variations of the manufacturing process. © 2022 Acoustical Society of America.

<https://doi.org/10.1121/10.0014180>

(Received 13 June 2022; revised 25 August 2022; accepted 2 September 2022; published online 23 September 2022)

[Editor: Michael R. Haberman]

Pages: 1901–1912

I. INTRODUCTION

Additive manufacturing (AM), also referred to as three-dimensional (3D) printing, is a manufacturing process in which the constituent materials are selectively placed in space to create customized objects with non-uniform properties, either by tailoring the internal structure of the objects (e.g., porosity, periodic lattices) or by varying the relative proportion of the deposited materials (e.g., functionally graded density and/or stiffness) (Mirzaali *et al.*, 2020). The diversity of AM technologies has led to a variety of processes capable of printing objects using material ingredients ranging from elastomers and polymers to metals. In particular, photopolymer-based AM has experienced a wide dissemination in engineering and science over the past years, and its versatility also has contributed to the field of acoustics (Naify *et al.*, 2022). This concerns not only biomedical applications, such as the prototyping of tissue-mimicking phantoms for ultrasound imaging system assessment (Cloonan *et al.*, 2014) or the conception of scaffolds intended for tissue engineering uses (Aliabouzar *et al.*, 2018), but also the design of passive components for wave front shaping applications, including backing material, lenses and matching layers for piezoelectric transducers

(Farinas *et al.*, 2016), acoustic holograms to correct transcranial focused ultrasound aberrations (Ferri *et al.*, 2019), and other metamaterials for wideband acoustic absorptions (Yang *et al.*, 2020).

Photopolymer-based AM is a layer-by-layer process and the properties of the produced samples depend on several characteristics, such as the mechanical properties of the material ingredients and their spatial arrangement, as well as the printing resolution, orientation, and post-processing (e.g., curing time and temperature) (Honarvar and Varvani-Farahani, 2020). Thereby, the achievement of complex materials and structures with specific acoustic responses relies on an accurate knowledge of the bulk acoustic properties of the elementary constituent materials. Within this context, a limited number of works have been carried out to report on the longitudinal bulk properties (i.e., phase velocity and attenuation) of photopolymer materials, as well as on their frequency dependence, by using different ultrasound methods, including a broadband reflection measurement technique using a focused single-element transducer (Jacquet *et al.*, 2015; Jacquet *et al.*, 2018), a two-sample substitution technique using a single-element broadband transducer as an emitter and a bilaminar hydrophone as a receiver (Bakaric *et al.*, 2021), and a pulse-echo technique using a linear transducer array for launching and detecting a wideband plane wave (Aghaei *et al.*, 2022). Although the

^{a)}Electronic mail: nicolas.bochud@u-pec.fr

reported longitudinal bulk properties are valuable towards ultrasound imaging and therapy purposes, emerging applications involving 3D-printed periodic micro-architected media also require the knowledge of the transverse bulk properties to account for possible coupling mechanisms (Fielder and Nair, 2022; Kruisová *et al.*, 2018). To date, however, transverse bulk properties are still lacking for such photopolymer materials in the MHz regime.

Notwithstanding, long before the recent democratization of 3D printing, several methods have been developed for measuring transverse waves propagating in other types of attenuating materials. In particular, measurements in oblique incidence have been proposed to exploit mode conversion along the liquid–solid interface, which can be achieved using either simple transmission (Pearson and Murri, 1987; Rokhlin and Wang, 1992; Wu, 1996) or double through-transmission (Chu and Rokhlin, 1994). However, the former method suffers from a significant drawback, because it needs two transducers and requires shifting the receiving transducer, since the wave path is modified due to refraction at the water–solid interface in oblique incidence. In contrast, the latter method requires a single transducer only (that acts both as an emitter and receiver), since the wave is transmitted through the solid, reflected by a plane reflector, and then travels back to the transducer after a second transmission through the solid. Therefore, the transducer remains fixed, as the wave follows the same path back and forth, regardless of the incident angle. Moreover, it has been shown that using the wave transmitted back and forth through the solid in normal incidence as a reference, instead of a wave transmitted through water, decreases the uncertainties on the measured transverse phase velocity and attenuation, which may arise from geometric sample imperfections and uncertainty on the water celerity (Chu and Rokhlin, 1994). Even more important, the double through-transmission method also reduces the amplitude differences between the different waves being compared. Indeed, for highly attenuating materials and especially for transverse wave propagation, this amplitude difference could be in the same order of magnitude than the dynamic range of the transducer, leading to weak signal to noise ratio (SNR) or signal distortion.

Here, we propose to adapt the double through-transmission method initially introduced by Chu and Rokhlin (1994), to extract not only the phase velocity of both longitudinal and transverse waves propagating in photopolymer materials, but also their attenuation, as well as the frequency dependence of these ultrasound characteristics. The investigated samples were manufactured using two different printing technologies—stereolithography (SLA) and multi-material polyjet—and included standard white and clear resins (uncured and cured), as well as mixtures made of varying volume fractions of a rigid glassy polymer and a compliant rubbery polymer. Overall, this approach was motivated by two main objectives. First, it allows for the quantitative assessment and comparison of the ultrasound properties of samples that undergo slight variations in

their manufacturing process, induced either by the curing or by the varying volume fractions. Second, it allows constituting a dataset of experimentally measured ultrasound characteristics for photopolymer materials, which will be valuable for the computational calibration and validation of models involving more complex spatial arrangements towards the design of programmable acoustic responses (Kruisová *et al.*, 2016; Loving *et al.*, 2018; Miniaci *et al.*, 2018).

The remainder of the paper is organized as follows: Sec. II revisits the theoretical principles and underlying hypotheses of the double through-transmission method in oblique incidence. Section III describes the additively manufactured samples, the ultrasound measurements setup, together with the dedicated signal processing steps used to extract the relevant ultrasound characteristics, and the method used for expressing the measurement uncertainties. The approach used to model the experimentally observed dispersion and attenuation, along with the inverse procedure used to identify a reduced number of intrinsic ultrasound parameters, is then introduced in Sec. IV. Finally, the obtained results, along with the strengths and limitations of the proposed approach, are discussed in Secs. V and VI, respectively.

II. DOUBLE THROUGH-TRANSMISSION METHOD IN OBLIQUE INCIDENCE

The proposed approach relies on two independent measurements only, which combine normal and oblique incidences, as schematically depicted in Fig. 1. In the general case, the measurement under oblique incidence would require the knowledge of the angles of propagation of the transmitted waves, denoted by θ_L for longitudinal waves and θ_T for transverse waves, which depend upon the angle of the incident wave, denoted by θ_i , according to Snell's law,

$$\frac{\sin \theta_L}{v_L} = \frac{\sin \theta_T}{v_T} = \frac{\sin \theta_i}{c_w}, \quad (1)$$

where v_L and v_T are the phase velocities of the longitudinal and transverse waves, respectively, and c_w is the water sound wave celerity.

Since both longitudinal and transverse waves would remain propagative for incident angles θ_i lower than the critical angle $\theta_i^{\text{cr}} = \arcsin(c_w/v_L)$, in the following, we focus on the specific case where only transverse waves can propagate (i.e., $\theta_i > \theta_i^{\text{cr}}$). In this case, the first measurement under normal incidence provides the displacements of the front face reflection $u_1(t)$, the back face reflection $u_2(t)$, and the double through-transmitted signal $u_3(t)$ [see Fig. 1(a)]. Likewise, the second measurement under oblique incidence provides the double through-transmitted signal $u_4(t)$ [see Fig. 1(b)].

The proposed method relies on several hypotheses. First, the attenuation in water is assumed to be negligible compared to that in the solid. Second, the distance d between the transducer and the solid, so as the distance D between the transducer and the reflector, are assumed to be very large compared to the sample thickness h . Thereby, since the method exploits different echoes with close wave

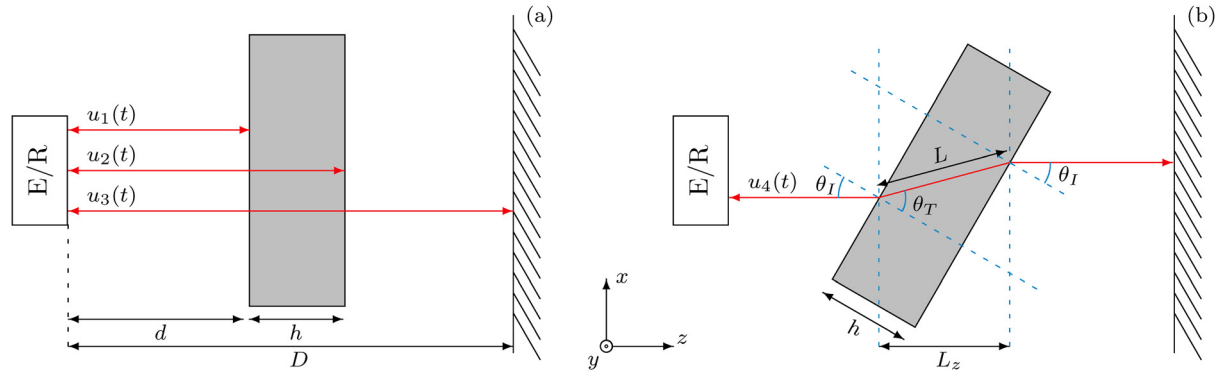


FIG. 1. (Color online) Schematic representation of the proposed double through-transmission method combining two measurements. (a) The measurement under normal incidence provides the front face reflection $u_1(t)$, the back face reflection $u_2(t)$, and the double through-transmitted signal $u_3(t)$. (b) the measurement under oblique incidence provides the double through-transmitted signal $u_4(t)$ for the specific case where only transverse waves are propagative. The solid, in gray, is placed in immersion between a single transducer [that acts both as an emitter (E) and receiver (R)] and the hard wall, which depicts the perfect reflector.

paths relative to one another, the contribution of diffraction effects can be neglected, and the acoustical field can be modeled under the plane wave assumption. Third, the duration of the pulse is assumed to be smaller than the time-of-flight of the wave traveling back and forth through the solid [i.e., h is sufficiently large to separate the echoes $u_1(t)$ and $u_2(t)$], which implies that there are neither constructive nor destructive interferences between the different echoes. Fourth, the solid is assumed to be isotropic.

Under those assumptions, the displacement components $u_i(t)$, with $i = 1, \dots, 4$, can be written in the Fourier domain as $U_i(\omega) = A_i(\omega) \exp(j\phi_i(\omega))$, where $A_i(\omega)$ and $\phi_i(\omega)$ denote the amplitude and phase spectra, respectively, j being the unit imaginary number. Hence,

$$\begin{aligned} U_1(\omega) &= A_1(\omega) \exp(j\phi_1(\omega)) \\ &= R_n(\omega) U_0(\omega) \exp(-2jk_w d), \end{aligned} \quad (2a)$$

$$\begin{aligned} U_2(\omega) &= A_2(\omega) \exp(j\phi_2(\omega)) \\ &= -R_n(\omega) T_n(\omega) U_0(\omega) \\ &\quad \times \exp(-2j(k_w d + k_L(\omega) h)), \end{aligned} \quad (2b)$$

$$\begin{aligned} U_3(\omega) &= A_3(\omega) \exp(j\phi_3(\omega)) \\ &= R_{\text{ref}}(\omega) T_n^2(\omega) U_0(\omega) \\ &\quad \times \exp(-2j(k_w(D - h) + k_L(\omega) h)), \end{aligned} \quad (2c)$$

$$\begin{aligned} U_4(\omega) &= A_4(\omega) \exp(j\phi_4(\omega)) \\ &= R_{\text{ref}}(\omega) T^2(\theta_I, \omega) U_0(\omega) \\ &\quad \times \exp(-2j(k_w(D - L_z) + k_T(\omega) L)), \end{aligned} \quad (2d)$$

where $U_0(\omega)$ is the spectrum of the emitted wave, $U_1(\omega)$, $U_2(\omega)$, $U_3(\omega)$ are the spectra of the echoes recorded in normal incidence [see Eqs. (2a)–(2c)], and $U_4(\omega)$ is the spectrum of the echo recorded in oblique incidence [see Eq. (2d)], which is given for the case where the angle of incidence $\theta_I > \theta_I^{\text{cr}}$ only. The wave number in water is denoted by $k_w = \omega/c_w$, whereas the longitudinal and

transverse wave numbers in the solid are denoted by $k_L(\omega)$ and $k_T(\omega)$, respectively. The water–solid and water–reflector reflection coefficients are denoted by $R_n(\omega)$ and $R_{\text{ref}}(\omega)$, respectively. The total transmission coefficient (that accounts for solid–water interfaces for both front and back faces) in normal incidence is given as

$$T_n(\omega) = \frac{4Z_w Z_L(\omega)}{(Z_w + Z_L(\omega))^2}, \quad (3)$$

where $Z_w = \rho_w c_w$ and $Z_L = \rho v_L(\omega)$ are the acoustic impedances of water and of the solid, ρ_w and ρ being their respective mass densities. In oblique incidence [recall Eq. (2d) and Fig. 1(b)], the distance $L = h/\cos(\theta_T)$ corresponds to the path of the wave into the solid and $L_z = L \cos(\theta_T - \theta_I)$ represents its projection along the z -axis (according to the orthonormal basis for the space depicted in Fig. 1). In such a case, since the angle of incidence $\theta_I > \theta_I^{\text{cr}}$, only transverse waves are propagative in the medium, so that the total transmission coefficient $T(\theta_I, \omega)$ can be derived from the continuity equations for stresses and displacements at both interfaces as in Royer and Dieulesaint (1999),

$$T(\theta_I, \omega) = \frac{4 \frac{Z_w \cos \theta_L}{Z_L(\omega) \cos \theta_I} \frac{v_T^2(\omega)}{v_L^2(\omega)} \sin 2\theta_L \sin 2\theta_T}{\left(\frac{v_T^2(\omega)}{v_L^2(\omega)} \sin 2\theta_L \sin 2\theta_T + \cos^2 2\theta_T + \frac{Z_w \cos \theta_L}{Z_L(\omega) \cos \theta_I} \right)^2}. \quad (4)$$

[See the supplementary material for the detailed calculations for retrieving the total transmission coefficient $T(\theta_I, \omega)$.¹] By combining Eqs. (2a) and (2b) and given that the wave number under normal incidence can be stated as $k_L(\omega) = \omega/v_L(\omega) - j\alpha_L(\omega)$, it is possible to recover the frequency-dependent phase velocity $v_L(\omega)$ and attenuation $\alpha_L(\omega)$ of the longitudinal wave as

$$v_L(\omega) = \frac{2h}{\Delta t_{12}(\omega)}, \quad (5a)$$

$$\alpha_L(\omega) = \frac{1}{2h} \ln \left(\left| \frac{T_n(\omega) A_1(\omega)}{A_2(\omega)} \right| \right), \quad (5b)$$

where $\Delta t_{12}(\omega) = (\varphi_1(\omega) - \varphi_2(\omega))/\omega$ is the frequency-dependent time-of-flight difference between $u_1(t)$ and $u_2(t)$, and $\ln(\cdot)$ denotes the natural logarithm of the quantity. In the same way, combining Eqs. (2c) and (2d), along with the previously derived expressions for $v_L(\omega)$ and $\alpha_L(\omega)$, further allow retrieving the frequency-dependent phase velocity $v_T(\omega)$ and attenuation $\alpha_T(\omega)$ of the transverse wave as

$$v_T(\omega) = \frac{1}{\cos \theta_T} \left(\frac{1}{v_L(\omega)} + \frac{1}{c_w} \left(\frac{\cos(\theta_T - \theta_I)}{\cos \theta_T} - 1 \right) + \frac{\Delta t_{34}(\omega)}{2h} \right)^{-1}, \quad (6a)$$

$$\alpha_T(\omega) = \alpha_L(\omega) \cos \theta_T + \frac{\cos \theta_T}{2h} \ln \left(\left| \frac{T^2(\theta_I, \omega) A_3(\omega)}{T_n^2(\omega) A_4(\omega)} \right| \right), \quad (6b)$$

where $\Delta t_{34}(\omega) = (\varphi_3(\omega) - \varphi_4(\omega))/\omega$ is the frequency-dependent time-of-flight difference between $u_3(t)$ and $u_4(t)$. By making use of Eq. (1), it can be shown that Eq. (6a) can be expressed independently of θ_T as¹

$$v_T(\omega) = \left(\left(\frac{\Delta t_{34}(\omega)}{2h} \right)^2 + 2 \frac{\cos \theta_I - 1}{c_w} \times \left(\frac{\Delta t_{34}(\omega)}{2h} + \frac{1}{v_L(\omega)} - \frac{1}{c_w} \right) + \frac{1}{v_L(\omega)} \frac{\Delta t_{34}(\omega)}{h} + \frac{1}{v_L^2(\omega)} \right)^{-1/2}. \quad (7)$$

In practice, one therefore first must solve Eq. (7), so that the angle θ_T can be subsequently obtained using Eq. (1). Finally, introducing the latter into Eqs. (4) and (6b) sequentially allows determining the total transmission coefficient $T(\theta_I, \omega)$ and the attenuation of the transverse wave $\alpha_T(\omega)$. It should also be noted that the phase velocity and attenuation measurements extracted with this method do not require the knowledge of $R_n(\omega)$ and $R_{\text{ref}}(\omega)$, since both reflection coefficients cancel out when solving the equations.

III. EXPERIMENTAL METHODS

A. Additively manufactured samples

Additive manufacturing of the photopolymer samples was achieved using two different commercially available 3D printers. A first set of samples was obtained using the Form3 3D printer (Formlabs, Somerville, MA), which is based on laser SLA. This printing technology consists of projecting an ultraviolet (UV) beam to accurately polymerize a liquid photosensitive resin contained in a transparent tray and thus, to manufacture a solid sample point-by-point

and layer-by-layer, with a resolution down to 50 μm . Two different resins have been employed in this study: white and clear resins, whose commercial names are White FLGPWH04 and Clear FLGPCL04, respectively. All samples have been subsequently washed in a stirring isopropanol tank (Form Wash, Formlabs) to remove unpolymerized resin. To improve the photopolymerization, an optional step consisted of applying UV light under a controlled temperature environment (Form Cure, Formlabs) to cure the samples. Curing time and temperature were selected according to the manufacturer's recommendations (60 and 30 min at 60° C for the white and clear resins, respectively). Altogether, four samples have been manufactured to investigate the impact of the resin type and of the curing process on the resulting ultrasound properties: uncured white (UW), cured white (CW), uncured clear (UC), and cured clear (CC). A second set of samples was obtained using the multi-material Objet 260 3D printer (Stratasys, Los Angeles, CA), which is based on polyjet technology. The latter consists of applying a layer-by-layer method where multiple streams of UV-curable photopolymers are jetted through printing nozzles onto a building tray (Zorzetto *et al.*, 2020). Two different photopolymers have been used here: a rigid glassy polymer [commercial name VeroWhitePlus (VW⁺)] and an elastomeric polymer [commercial name TangoBlackPlus (TB⁺)]. Unlike SLA, such a multi-material inkjet-based process allows blending highly dissimilar photopolymers at the microscale (voxel with side length of around 40 μm) to subsequently obtain macroscopically homogeneous samples with any intermediate volume fraction, V_f . In this study, four different volume fractions of TB⁺ have been tested, i.e., 0%, 5%, 10%, and 18%.

All samples were 3D-printed as homogeneous plate-like samples. Their dimensions were set to 70 × 35 × h mm³ along the x , y , and z directions. The dimensions in the xy -plane were chosen so that they cover the entire emission surface of the transducer, even for angles of incidence larger than the critical angle θ_I^{cr} (recall Fig. 1). The thickness h of each sample was chosen based on two criteria. First, the sample had to be thick enough to ensure a temporal separation of the measured echoes $u_1(t)$ and $u_2(t)$. Second, it had to be thin enough to ensure a sufficient double through-transmission across the sample [i.e., $u_3(t)$ and $u_4(t)$], and thus to avoid a too low SNR due to attenuation, especially for transverse waves [i.e., $u_4(t)$]. Thereby, the nominal value for the samples' thickness ranged from about 3.8–4.6 mm depending upon the manufacturing process and the volume fraction of TB⁺. To account for the statistical dispersion, the dimensions and mass of the samples were measured eight times each using a digital caliper (± 0.01 mm) and a precision balance (± 1 mg), respectively.

B. Ultrasound measurements

All measurements were performed using a multielement probe (Imasonic SAS, Voray sur l'Ognon, France) driven by programmable multi-channel electronics (Advanced OEM Solutions, WestChester, USA). This type of device, initially

devoted to medical imaging, has recently also been used to characterize the ultrasound properties of photopolymer materials (Aghaei *et al.*, 2022). Measurements were performed using a linear transducer array consisting of 32 elements. Each element had a width and a height of 0.5 and 12 mm, respectively, yielding a total transmission surface of $16 \times 12 \text{ mm}^2$. The transducer operated at a central frequency $f_c = 2.25 \text{ MHz}$ (−18 dB frequency bandwidth from 1.15–3.15 MHz) and the pitch of the array was 0.5 mm. Measurements were carried out in immersion using a plane wave imaging mode, by simultaneously emitting a pulse on all elements. It should be noted that the wavelength in water (i.e., $\lambda_w = c_w/f_c \approx 0.67 \text{ mm}$ at the central frequency) was small compared to the lateral dimension of the transducer, which implies a high directivity factor and a weak geometric attenuation that further support the assumption of negligible diffraction. The signals were recorded during $200 \mu\text{s}$ (from 150–350 μs after the pulse emission), digitized with a sample frequency $f_s = 100 \text{ MHz}$ and quantized with a 12 bit resolution. The temperature during the measurements was 20°C (measured using a Zacro LCD digital thermometer, with a resolution of $\pm 0.1^\circ \text{C}$), so that the water celerity could be estimated using Marczak's polynomial model (Marczak, 1997). Each sample was measured under normal and oblique incidences by rotating the sample using a motorized rotation stage ($\pm 1^\circ$). In oblique incidence, the angle of incidence was set to $\theta_I = 50^\circ$ as it ensured that $\theta_I > \theta_I^{\text{cr}}$ for all samples and allowed maximizing the total transverse transmission coefficient [recall Eq. (4)]. Optimal azimuthal alignment was obtained under normal incidence by minimizing the time-of-flight difference between the front face reflected signals received on the leftmost and rightmost elements of the array. Optimal vertical alignment was achieved by maximizing the SNR of the reflected signals. Each measurement was repeated eight times to account for the statistical dispersion of the frequency-dependent time-of-flight durations [i.e., $\Delta t_{12}(\omega)$ and $\Delta t_{34}(\omega)$] and amplitude ratios [i.e., $A_1(\omega)/A_2(\omega)$ and $A_3(\omega)/A_4(\omega)$]. Between each measurement repetition, the sample has been turned over and around, and the alignment was repeated to account for possible geometrical imperfections of the sample.

C. Signal processing

To extract ultrasound characteristics, i.e., the phase velocities, $v_L(\omega)$ and $v_T(\omega)$, and attenuations, $\alpha_L(\omega)$ and $\alpha_T(\omega)$, from the measurements, a dedicated signal processing approach has been developed. First, to cancel out any spurious signals and improve the SNR, the signals recorded on the 32 elements of the transducer were averaged. To serve as an example, the resulting averaged displacement components $u_i(t)$, with $i = 1, \dots, 4$, are depicted in Fig. 2 for one measurement performed on the CC sample.

Note that the reflected signal $u_2(t)$ is upside-down with respect to the other signals due to the negative reflection coefficient at the sample-water interface and its sign should therefore be inverted before applying further processing. Second, the central time t_i of each signal $u_i(t)$ was calculated based on the maximum of the signal envelop, i.e., the time for which the modulus of the Hilbert transform is maximal. To isolate the echoes of interest, a tapered cosine window (i.e., a Tukey window with a tapered fraction of 50%), centered on t_i and of time length $t_2 - t_1$ was applied to each signal $u_i(t)$. Third, a fast Fourier transform was then applied to each signal $u_i(t)$ over the total acquisition time length, thereby including zero padding as a typical way to improve the spectrum resolution. Fourth, to reduce the 2π -ambiguity due to the phase unwrapping, the absolute phase was calculated as in Niemi *et al.* (2005) and He and Zheng (2001). In this way, each signal $u_i(t)$ was circularly shifted to the beginning of the window, so that the total phase spectrum can be written as

$$\varphi_i(\omega) = \omega t_i + \phi_i(\omega), \quad (8)$$

where ωt_i is the linear part of the phase related to the temporal shift and $\phi_i(\omega)$ is the phase spectrum of the shifted signal, which naturally lies between $-\pi$ and π . The resulting amplitude and shifted phase spectra of each of the four signals $u_i(t)$ are depicted in Fig. 3 for the CC sample.

Fifth, the frequency-dependent time-of-flight durations $\Delta t_{12}(\omega)$ and $\Delta t_{34}(\omega)$, along with the amplitude ratios $A_1(\omega)/A_2(\omega)$ and $A_3(\omega)/A_4(\omega)$, can then be easily calculated and introduced into Eqs. (5a), (5b), (6b), and (7) to recover the frequency-dependent phase velocity and

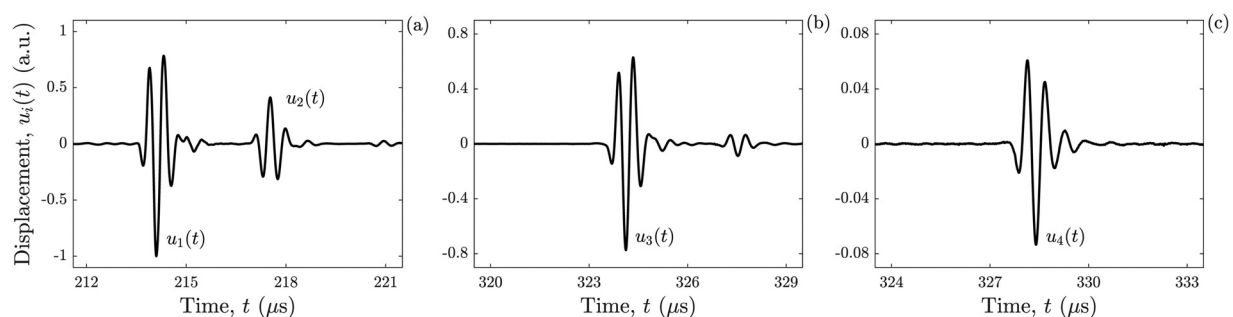


FIG. 2. Overview of the recorded signals for the CC sample, where the four echoes correspond to those depicted in Fig. 1. (a) Front face reflection $u_1(t)$ and back face reflection $u_2(t)$ measured in normal incidence, (b) double through-transmitted signal $u_3(t)$ measured in normal incidence, and (c) double through-transmitted signal $u_4(t)$ measured in oblique incidence at $\theta_I = 50^\circ$.

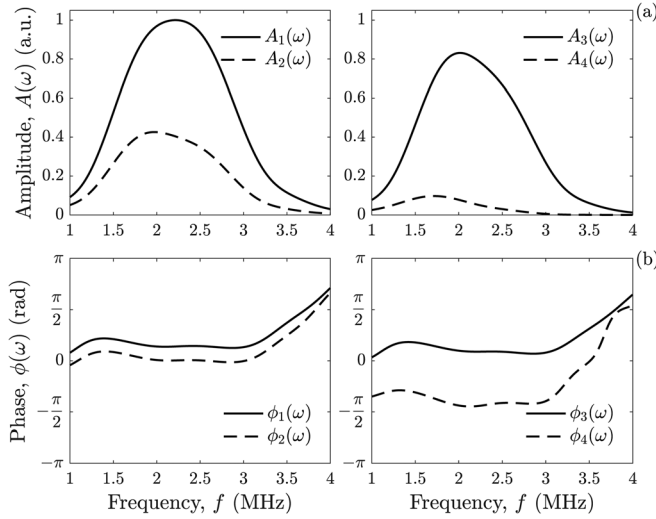


FIG. 3. (a) Amplitude and (b) shifted phase spectra corresponding to the four time-domain signals depicted in Fig. 2 for the CC sample.

attenuation of both the longitudinal and transverse waves (see Fig. 4). As can be observed, the phase velocities slightly increase with frequency, while the attenuations exhibit a quasi-linear frequency dependence over the useful frequency bandwidth. Note that similar trends were already consistently evidenced in Bakaric *et al.* (2021) and Aghaei *et al.* (2022) for photopolymers, but these studies were limited to longitudinal waves only.

D. Measurement uncertainty

The measurement uncertainty was evaluated following the recommendations of the guide to the expression of uncertainty in measurement (BIPM, IEC, IFCC, ILAC, ISO, IUPAC, IUPAP, and OIML, 2008). As the frequency-dependent times of flight durations [$\Delta t_{12}(\omega)$ and $\Delta t_{34}(\omega)$]

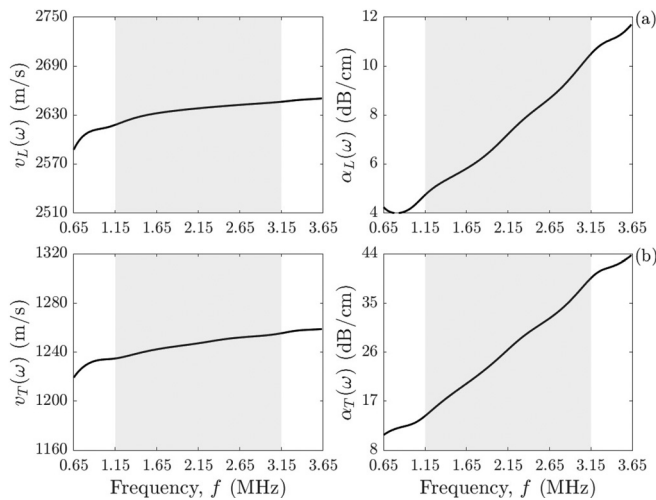


FIG. 4. Ultrasound characteristics for the CC sample obtained after applying the dedicated signal processing steps. (a) Longitudinal phase velocity $v_L(\omega)$ and attenuation $\alpha_L(\omega)$, (b) transverse phase velocity $v_T(\omega)$ and attenuation $\alpha_T(\omega)$. The gray area represents the -18 dB frequency bandwidth of the transducer.

and amplitude ratios [$A_1(\omega)/A_2(\omega)$ and $A_3(\omega)/A_4(\omega)$], together with the sample dimensions and mass, resulted from independent observations, their respective standard uncertainties were assessed using type A evaluation of standard uncertainty. Conversely, as the incidence angle θ_i and the water sound celerity c_w depended on the rotating stage and digital thermometer resolutions, their standard uncertainties were assessed using type B evaluation of standard uncertainty. The standard uncertainty on each input quantity was modeled as a Gaussian probability distribution. The combined standard uncertainty on the ultrasound characteristics, i.e., phase velocities and attenuations, was then evaluated by means of Monte Carlo's method for computing the law of propagation of uncertainty for uncorrelated input quantities (Papadopoulos and Yeung, 2001), using 10 000 random values for each input distribution and for each discrete frequency. Finally, all uncertainties reported in the following correspond to expanded uncertainties, given with a 95% confidence level (i.e., obtained by multiplying the combined standard uncertainty with a coverage factor $k = 1.96$). Note that the water density ρ_w was set equal to 998 kg/m^3 and not accounted for in the expression of uncertainty.

IV. MECHANICAL MODELING

A. Szabo wave equation

The complex viscoelastic behavior of some materials (e.g., photopolymers, biological tissues) exhibits dispersive losses that cannot be accurately captured by the classical rheological Voigt model, which relies on an acoustic attenuation proportional to ω^2 . The heterogeneous nature of such materials indeed suggests that their viscous behavior involves more complex phenomena, such as multiple relaxation times for which individual relaxation processes cannot be easily identified (Näsholm and Holm, 2011). Therefore, several approximated phenomenological models have been proposed to describe wave dispersion and attenuation in such media (Holm *et al.*, 2013). Among these models, an appealing approach consists of describing the frequency-dependent attenuation with a power law as

$$\alpha_M(\omega) = \alpha_{1M} \omega^{y_M}, \quad (9)$$

where the subscript M stands either for longitudinal (L) or transverse (T) waves. The constant attenuation α_{1M} can be expressed in $\text{dB/m}/(\text{rad.MHz})^{y_M}$ with y_M being a dimensionless exponent, which usually lies within the range 0–2. In particular, the *ad hoc* model proposed by Szabo and Wu (2000) allows recovering such power law expression for the attenuation by introducing a fractional time derivative into the one-dimensional wave equation as

$$\frac{\partial^2 u_M(z,t)}{\partial z^2} - \frac{2\alpha_{1M}}{v_{0M} \cos(y_M \pi/2)} \frac{\partial^{y_M+1} u_M(z,t)}{\partial t^{y_M+1}} = \frac{1}{v_{0M}^2} \frac{\partial^2 u_M(z,t)}{\partial t^2}, \quad (10)$$

where v_{0M} states for the bulk wave velocity of either longitudinal ($M = L$) or transverse ($M = T$) waves. In addition,

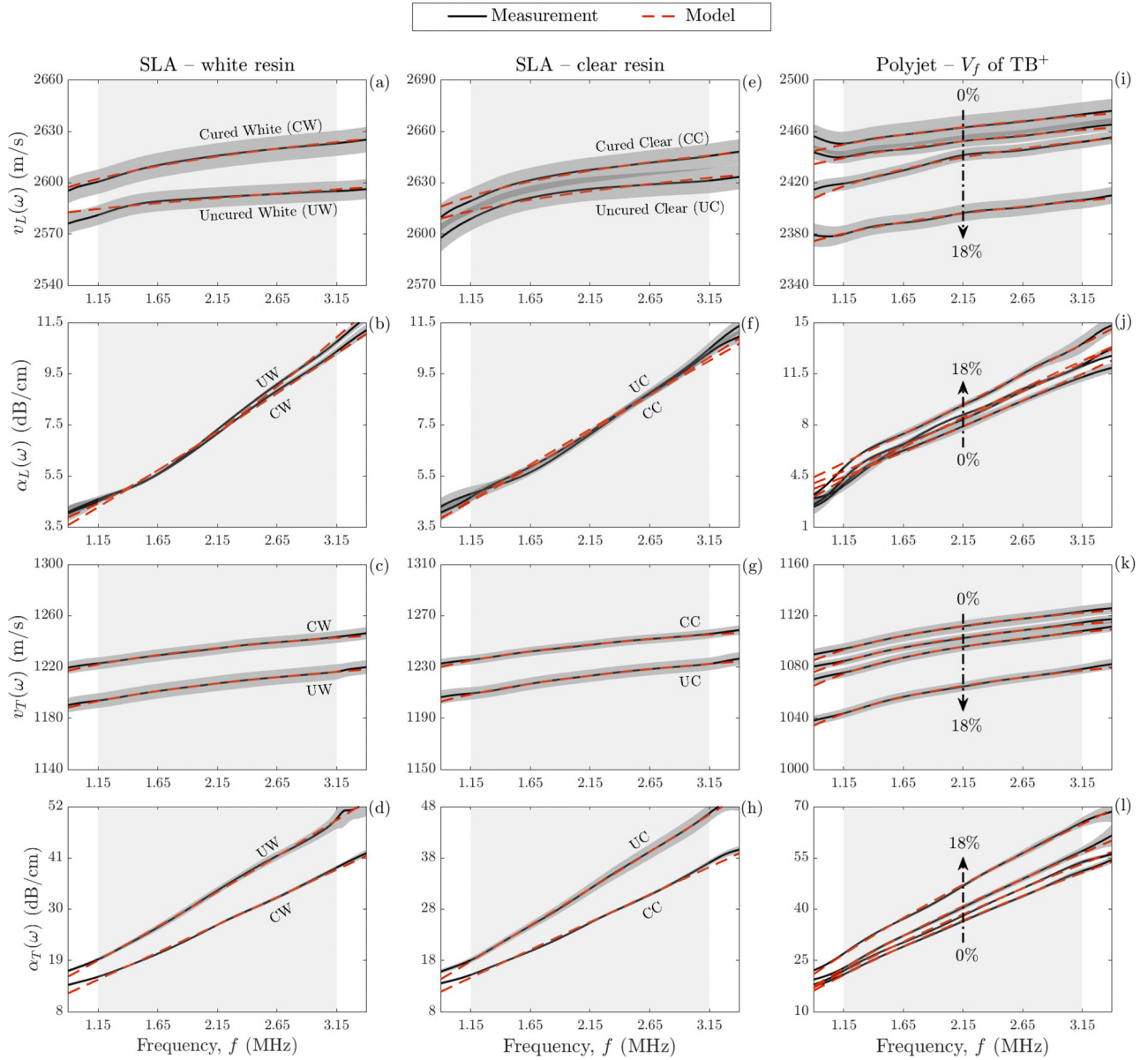


FIG. 5. (Color online) Measured ultrasound characteristics (continuous black lines): (a) longitudinal phase velocity $v_L(\omega)$, (b) transverse phase velocity $v_T(\omega)$, (c) longitudinal attenuation $\alpha_L(\omega)$, and (d) transverse attenuation $\alpha_T(\omega)$ for the uncured (UW) and cured (CW) samples printed with the white resin. In the same way, panels (e) to (h) display the results for the uncured (UC) and cured (CC) samples printed with the clear resin. Likewise, panels (i) to (l) display the results for the multi-material samples with varying V_f of TB^+ . The dashed red lines correspond to the model outcomes calculated using the optimal model parameter $\hat{\theta}_M$. The dark gray areas display the expanded uncertainties on the results, while the light gray area shows the useful frequency bandwidth on which the inversion process was performed.

because Szabo's model is causal—in the sense that it satisfies Kramer–Kronig relationships (O'Donnell *et al.*, 1981)—it also predicts that the frequency variations of the phase velocity are not independent from the attenuation. Therefore, considering plane wave propagation, i.e., $u_M(t) = A \exp(j(\omega t - k_M z))$, allows deriving the dispersion relation from Eq. (10) as

$$k_M(\omega) = \sqrt{\frac{\omega^2}{v_{0M}^2} - (j\omega)^{y_M+1} \frac{2\alpha_{1M}}{v_{0M} \cos(y_M \pi/2)}}. \quad (11)$$

According to Kelly *et al.* (2008), assuming that $\alpha_{1M}/\cos(y_M \pi/2) \ll 1$ allows simplifying this expression to

$$k_M(\omega) = \frac{\omega}{v_{0M}} - j \frac{\alpha_{1M}(j\omega)^{y_M}}{\cos(y_M \pi/2)}. \quad (12)$$

By invoking the de Moivre's identity for $\pi/2$, i.e., $j^{y_M} = \cos(y_M \pi/2) + j \sin(y_M \pi/2)$, the real part of Eq. (12) allows identifying the phase velocity $v_M(\omega)$ as

$$v_M(\omega) = \frac{\omega}{\Re(k_M(\omega))} = \left(\frac{1}{v_{0M}} + \alpha_{1M} \tan(y_M \pi/2) \omega^{y_M-1} \right)^{-1}, \quad (13)$$

whereas its imaginary part, i.e., $-\Im(k_M(\omega))$, allows retrieving the power law attenuation given by Eq. (9). It should be noted

that this model exhibits a mathematical singularity for $y_M = 1$. For such a case, modified expressions for the phase velocity and attenuation can be found in Szabo and Wu (2000). Overall, this phenomenological model is valid for an intermediate frequency range only. In particular, if the main cause of attenuation is suspected to be related to relaxation phenomena, one would expect the attenuation to be proportional to ω^2 in the low frequency regime and to tend towards an asymptotic value in the high frequency regime (Nachman *et al.*, 1990). To account for this, Szabo and Wu (2000) proposed to incorporate an additional model parameter $\alpha_{0M} = \alpha_M(0) \neq 0$ into Eq. (9) to correct for the eventual attenuation offset at the frequency $\omega = 0$. Doing so, the phase velocity expression [Eq. (13)] remains identical, while the power law attenuation now becomes

$$\alpha_M(\omega) = \alpha_{0M} + \alpha_{1M}\omega^{y_M}. \quad (14)$$

More conveniently, $v_M(\omega)$ and $\alpha_M(\omega)$ can also be expressed as a function of a reference frequency ω_c , where one can deliberately choose $\omega_c = 2\pi f_c$ (Bakaric *et al.*, 2021), so that

$$v_M(\omega) = \left(\frac{1}{v_{cM}} + (\alpha_{cM} - \alpha_{0M}) \tan(y_M \pi/2) \right. \\ \left. \times \left(\left(\frac{\omega}{\omega_c} \right)^{y_M} \omega^{-1} - \omega_c^{-1} \right) \right)^{-1}, \quad (15a)$$

$$\alpha_M(\omega) = \alpha_{0M} + (\alpha_{cM} - \alpha_{0M}) \left(\frac{\omega}{\omega_c} \right)^{y_M}, \quad (15b)$$

where $v_{cM} = v_M(\omega_c)$ and $\alpha_{cM} = \alpha_M(\omega_c)$. Although strictly equivalent mathematically, in practice, relations (15a) and (15b) are more convenient than Eqs. (13) and (14) to subsequently compare different materials. Indeed, for the latter, a small variation of y_M could lead to a large variation of α_{1M} , thereby potentially leading to a misidentification of the model parameters.

B. Identification of the model parameters

To extract quantitative information from the measured ultrasound characteristics that may allow for a reliable comparison of the viscoelastic behavior of the investigated samples, we propose an optimization procedure to identify, for each wave polarization M , the four model parameters $\theta_M = [v_{cM}, \alpha_{cM}, y_M, \alpha_{0M}]$ that minimize the following objective function $F(\theta_M)$ in a least squares sense as in Aghaei *et al.* (2022):

$$F(\theta_M) = \sqrt{\frac{1}{N} \sum_{n=1}^N \left| \frac{k_M(\omega_n) - k_M(\omega_n; \theta_M)}{k_M(\omega_n)} \right|^2}, \quad (16)$$

where $k_M(\omega_n) = \omega_n/v_M(\omega_n) - j\alpha_M(\omega_n)$ and $k_M(\omega_n, \theta_M)$ are the measured and modeled complex wave numbers at the n th discrete frequency, respectively, while N is the total number

of discrete frequencies of the useful bandwidth on which the optimization is performed (recall the gray area in Fig. 4). The minimization was performed using the unconstrained Simplex algorithm (Nelder and Mead, 1965), which was implemented in Python 3.8 (Python Software Foundation, Beaverton, OR). Formally, the optimal model parameters result from

$$\hat{\theta}_M = \arg \min_{\theta_M} (F(\theta_M)), \quad (17)$$

where the uniqueness of the solution was ensured by verifying the algorithm's convergence towards $\hat{\theta}_M$ for different initial guesses θ_M .

V. RESULTS

The matching between the measured ultrasound characteristics and the corresponding model outcomes calculated using the optimal model parameter $\hat{\theta}_M$ is depicted in Fig. 5 for the 3D-printed samples manufactured using SLA [panels (a)–(d) and (e)–(h) for the white and clear resin, respectively] and multi-material polyjet [panels (i)–(l)]. As can be observed, for all the investigated samples, the measured phase velocity of the transverse waves $v_T(\omega)$ is, as expected, systematically more than twice lower than that of the longitudinal waves $v_L(\omega)$ over the useful frequency bandwidth (light gray area in Fig. 5). Likewise, the attenuation of the transverse waves $\alpha_T(\omega)$ is almost four times higher than that of the longitudinal waves $\alpha_L(\omega)$. In addition, the relative expanded uncertainties (dark gray area) show that the proposed measurement method is very accurate, being able to discriminate very small variations of the phase velocity $v_M(\omega)$ (less than 1% for both polarizations M) and of the attenuation $\alpha_M(\omega)$ (less than 5% for both polarizations M) within the 95% limits of agreement.

Moreover, the modeled frequency-dependent ultrasound characteristics (dashed red lines) resulting from the identification inverse problem are in very good agreement with the experimental ones (continuous black lines). Indeed, the pseudo- R^2 , calculated as recommended by Kvålseth (1985) for a nonlinear regression analysis, are systematically higher than 0.99 for both the phase velocity $v_M(\omega)$ and attenuation $\alpha_M(\omega)$ over the useful frequency bandwidth (no matter the polarization M and the manufacturing process), except for the longitudinal phase velocity $v_L(\omega)$ of the uncured samples [$R^2 = 0.92$ and $R^2 = 0.94$ for the UW and UC samples depicted in panels (a) and (e), respectively].

To get a deeper insight into the inter- and intra-manufacturing process variability, Fig. 6 provides a comparison between the measured ultrasound characteristics (at the central frequency ω_c) and the corresponding optimal model parameters $\hat{\theta}_M$ for all the investigated samples. First, with regard to the inverse problem solutions, the retrieved values for the optimal model parameters \hat{v}_{cM} and $\hat{\alpha}_{cM}$ (red bins in Fig. 6) are in excellent agreement with the ultrasound characteristics measured at the central frequency ω_c , i.e., $v_M(\omega_c)$ and $\alpha_M(\omega_c)$ (dark gray bins), as they always fall within the 95% limits of agreement, as defined by the expanded

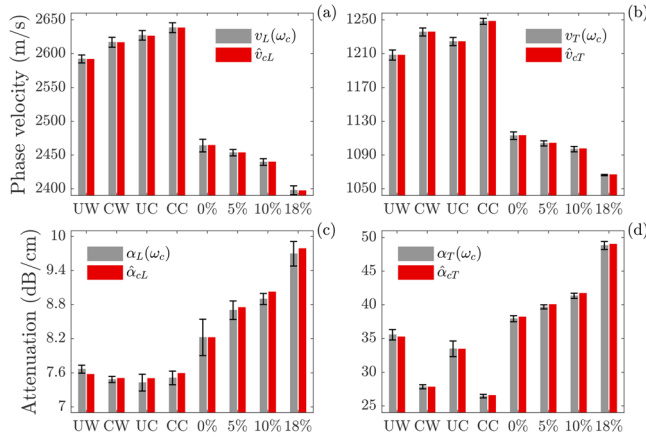


FIG. 6. (Color online) Comparison between the measured ultrasound characteristics (at the central frequency ω_c) across all samples (gray bars), together with their corresponding optimal model parameters (red bars): (a) longitudinal phase velocities, $v_L(\omega_c)$ and \hat{v}_{cL} , (b) transverse phase velocities, $v_T(\omega_c)$ and \hat{v}_{cT} , (c) longitudinal attenuations, $\alpha_L(\omega_c)$ and $\hat{\alpha}_{cL}$, and (d) transverse attenuations, $\alpha_T(\omega_c)$ and $\hat{\alpha}_{cT}$. The error bars displayed for the measured characteristics correspond to the expanded uncertainties.

uncertainties (error bars). As can be observed, the phase velocities $v_M(\omega_c)$ and attenuation $\alpha_M(\omega_c)$ of the samples manufactured with polyjet are respectively lower and higher than those of the samples manufactured with SLA. The reader is referred to Table I (given in Appendix A), which reports the detailed values of the measured ultrasound characteristics and of the optimal model parameters $\hat{\theta}_M$ recovered using Szabo's model.

Second, it is noteworthy that all 3D-printed samples manufactured using SLA (UW, CW, UC, and CC) exhibit very close ultrasound properties for the longitudinal waves, as the phase velocities \hat{v}_{cL} and attenuations $\hat{\alpha}_{cL}$ fall within the range of 50 m/s and 0.1 dB/cm only, respectively, which

represent less than a 2% relative variation with respect to the mean value. In contrast, for the transverse waves, the phase velocity \hat{v}_{cT} shows a relative increase higher than 3% between the softest (UW) and stiffest (CC) sample, and likewise the attenuation $\hat{\alpha}_{cT}$ shows a relative decrease of about 25%. Moreover, the curing process induces a slight increase in the longitudinal phase velocity \hat{v}_{cL} (1% and 0.5% for the white and clear resin, respectively), and this becomes more important for the transverse phase velocity \hat{v}_{cT} (2.3% and 2% for the white and clear resin, respectively). Although there are no significant differences for the longitudinal attenuation $\hat{\alpha}_{cL}$, the curing has a significant impact on the transverse attenuation $\hat{\alpha}_{cT}$ (a reduction of about 20% for both resins). Although its underlying physical interpretation is beyond the scope of this paper, it should be noted that the curing process also has an impact on the frequency-dependence of the attenuation $\alpha_M(\omega)$, as it is systematically correlated with a drop of the two remaining model parameters, i.e., \hat{y}_M and $\hat{\alpha}_{0M}$, no matter the wave polarization.

Third, for the four 3D-printed samples manufactured using multi-material polyjet (0%, 5%, 10%, and 18%), for both wave polarizations M , the phase velocity \hat{v}_{cM} consistently decreases, and likewise, the attenuation $\hat{\alpha}_{cM}$ increases, as a function of increasing volume fraction V_f of TB⁺. These trends are even more pronounced for the transverse waves' characteristics, and especially for the transverse attenuation $\hat{\alpha}_{cT}$ (relative increase of about 30%). As can be observed, there is no significant trend between the volume fraction V_f and the model parameters \hat{y}_M and $\hat{\alpha}_{0M}$ for these samples. Nevertheless, the frequency-dependence of the attenuation $\alpha_M(\omega)$, driven by the exponent y_M , significantly changes with the polarization M . It is quasi-linear for the longitudinal waves and approximately proportional to $\omega^{0.7}$ for the transverse waves.

TABLE I. Comparison between the measured phase velocities and attenuations at the central frequency ω_c , i.e., $v_M(\omega_c)$ and $\alpha_M(\omega_c)$, and the optimal model parameters $\hat{\theta}_M$ identified using Szabo's model. The uncertainties on the measured ultrasound characteristics correspond to the extended standard uncertainties (expressed with a 95% confidence level).

	Mass density ρ (kg/m ³)	M	Measurements at ω_c		Model parameters $\hat{\theta}_M$			
			$v_M(\omega_c)$ (m/s)	$\alpha_M(\omega_c)$ (dB/cm)	\hat{v}_{cM} (m/s)	$\hat{\alpha}_{cM}$ (dB/cm)	\hat{y}_M (–)	$\hat{\alpha}_{0M}$ (dB/cm)
UW	1168.9 ± 1.5	L	2592.0 ± 5.9	7.67 ± 0.07	2591.6	7.58	1.559	2.72
		T	1208.2 ± 6.0	35.53 ± 0.78	1208.1	36.12	1.344	8.53
CW	1171.7 ± 2.7	L	2616.7 ± 7.3	7.48 ± 0.05	2616.4	7.50	1.101	1.32
		T	1235.6 ± 4.7	27.84 ± 0.31	1235.7	27.82	1.014	1.60
UC	1168.1 ± 3.6	L	2627.0 ± 7.1	7.43 ± 0.15	2626.0	7.50	1.140	1.87
		T	1224.2 ± 4.9	33.44 ± 1.16	1224.2	33.41	1.044	2.47
CC	1166.8 ± 3.4	L	2638.4 ± 7.3	7.51 ± 0.12	2638.1	7.59	0.931	1.04
		T	1248.2 ± 3.6	26.45 ± 0.27	1248.4	26.56	0.977	1.77
0%	1182.8 ± 1.8	L	2464.0 ± 9.4	8.22 ± 0.32	2464.4	8.22	1.098	0.94
		T	1112.9 ± 4.5	37.92 ± 0.45	1113.2	38.18	0.712	–7.84
5%	1174.5 ± 2.0	L	2453.5 ± 4.8	8.70 ± 0.16	2453.5	8.75	1.151	1.43
		T	1103.8 ± 3.1	39.68 ± 0.31	1104.2	40.04	0.735	–7.03
10%	1174.3 ± 1.7	L	2439.6 ± 5.0	8.90 ± 0.10	2439.7	9.02	1.040	0.70
		T	1096.9 ± 3.2	41.33 ± 0.39	1097.5	41.70	0.733	–7.50
18%	1169.2 ± 1.8	L	2397.7 ± 6.6	9.69 ± 0.22	2397.1	9.79	1.062	1.12
		T	1066.2 ± 3.7	48.82 ± 0.59	1066.7	49.01	0.718	–9.16

VI. DISCUSSION

In this study, we proposed a double through-transmission method in oblique incidence for the nondestructive characterization of additively manufactured samples by ultrasound. The samples were fabricated using two different 3D-printing technologies, with the aim of identifying variations of the manufacturing process on their acoustic behavior (i.e., dispersion and attenuation). The set of samples printed with SLA was used to assess the impact of the curing process on two different resin types, while the set of samples printed using multi-material polyjet was used to assess the impact of the relative proportions of two photopolymers. All samples were first experimentally characterized to extract the frequency-dependent ultrasound characteristics, i.e., phase velocity and attenuation, of both longitudinal and transverse waves in the MHz regime. Second, a model-based inverse procedure has been proposed to quantitatively assess and compare the experimental evidence (dispersion, attenuation, etc.) observed on the different samples, as it allowed identifying a reduced number of intrinsic model parameters (i.e., four for each wave polarization).

The main findings were as follows: First, the proposed measurement method allowed us not only to recover longitudinal ultrasound characteristics, but also the transverse phase velocity and attenuation, as well as their frequency dependence. A detailed analysis of the experimental uncertainties showed that this method was able to accurately capture very small relative variations of these characteristics across the samples (less than 1% and 5% for the phase velocities and attenuation, respectively). Altogether, the ultrasound characteristics, and especially the ones related to the transverse waves, were shown to be very sensitive to the samples stiffening induced either by the curing process (for SLA) or by the decreasing relative proportion of TB⁺ (for multi-material polyjet). Second, the experimentally assessed frequency-dependent attenuation evidenced that the viscoelastic behavior of this class of photopolymers cannot be described by a simple rheological Voigt model. Nevertheless, this behavior could be adequately captured using a phenomenological model, which relies on the Szabo wave equation. This model allowed predicting that the observed dispersion can be explained by the measured attenuation. The identified intrinsic model parameters were in excellent agreement with the measurements, thereby demonstrating that such acoustic behavior can be predicted with a reduced number of parameters only.

A direct quantitative comparison with earlier reported longitudinal bulk properties (i.e., phase velocity and attenuation) is difficult, since the applied measurement technique, in particular the explored frequency regime, along with the investigated AM materials, often differ from one study to another. For instance, *Jacquet et al. (2018)* reported values of 2581.0 ± 33.3 m/s and 97.5 ± 20.1 dB/cm for the phase velocity and attenuation of VW⁺ evaluated at 20 MHz. In another related study, *Bakaric et al. (2021)* reported values of 2591 m/s and 6.02 dB/cm for the phase velocity and

attenuation of CC evaluated at 2 MHz, and likewise, values of 2495 m/s and 8.24 dB/cm for the phase velocity and attenuation of VW⁺. In a previous study by our group (*Aghaei et al., 2022*), which was related to samples with intermediate volume fractions (i.e., mixtures of VW⁺ and TB⁺) assessed in normal incidence only, we reported values of 2452 m/s and 8.01 dB/cm for the phase velocity and attenuation of VW⁺ evaluated at 2.25 MHz, and likewise, values of 2439 m/s and 9.33 dB/cm for the phase velocity and attenuation of a sample with a volume fraction equal to 10% of TB⁺. Extrapolating our estimates $\hat{\theta}_L$ to these frequencies yield (1) values of 2450.9, 2464.4, and 2521.1 m/s (7.82, 8.22, 81.1 dB/cm) for the phase velocity (attenuation) of VW⁺ at 2, 2.25, and 20 MHz, respectively; (2) values of 2635.1 m/s and 6.91 dB/cm for the phase velocity and attenuation of CC at 2 MHz; and (3) values of 2439.7 m/s and 9.02 dB/cm for the phase velocity and attenuation of the sample with a volume fraction equal to 10% of TB⁺ at 2.25 MHz. These longitudinal bulk properties are all in excellent agreement with the reported literature values, thus indicating that our modeling assumptions are reasonable for a wide frequency band.

In contrast, to the best of our knowledge, there is only one study (*Livingston et al., 2015*), which attempted to measure both longitudinal and transverse waves propagating in an AM material (VW⁺, polyjet technology) similar to ours. However, although the reported anisotropic values for the longitudinal phase velocities evaluated at 1 MHz (from 2460.6–2526.8 m/s) were in close agreement to ours (2442.3 m/s, after extrapolation to the same frequency), the values for the transverse phase velocities were surprisingly higher (from 1507.3–1781.7 m/s compared to 1088.6 m/s) and varied by more than 50% over the explored frequency bandwidth (0.5–1.6 MHz). Moreover, these values even exceeded the longitudinal phase velocities at lower frequencies (<0.7 MHz), which may be due to the inherent 2π -ambiguity in the phase unwrapping. The knowledge of the longitudinal and transverse phase velocities also allows determining the absolute value of the Poisson's ratio ν , which for all eight AM materials investigated here, ranges from 0.355–0.376. Knowing furthermore their mass density (see Table I in *Appendix A*) also allows us to determine their Young's modulus E , which ranges from 3.66–4.94 GPa. Although not directly comparable, the reported engineering moduli are in good agreement with values obtained by ultrasound guided waves for 3D-printed samples manufactured using the fused deposition modeling method (*Jäger et al., 2017*). It should be noted, however, that the derived values for the Young's modulus at 2.25 MHz are more than twice higher than those reported by the manufacturer (1.6 and 2.8 GPa for both white and clear resins, before and after curing, respectively, and 2.5 GPa for VW⁺), thus suggesting that the dynamic mechanical behavior of photopolymer materials in the MHz regime is significantly different from its quasi-static mechanical behavior.

Despite these promising results, our study suffers from some limitations. First, the samples fabricated using the

multi-material polyjet 3D printing technology were limited to a relatively low volume fraction of the elastomeric photopolymer (i.e., 18% of TB^+). According to our results, accurate transverse wave measurements performed using the double through-transmission method in oblique incidence should still be achievable for a volume fraction around 50% of TB^+ , but this would require fine-tuning the sample dimensions and the angle of incidence [see Fig. 1(b)]. Above such a volume fraction, mode conversion would be hardly manageable according to Snell's law [recall Eq. (1)]. Nevertheless, complementary measurements using a contact pulse-echo method with a shear transducer could allow circumventing this issue (Zhang *et al.*, 2019). Second, given that the ratio between the wavelength and the printing resolution (a few tenths of micrometers for both technologies) was large, all samples were assumed to be isotropic. Although the proposed method has proven feasible to determine phase velocities in anisotropic materials (Chu and Rokhlin, 1994), it would have to be adapted for measuring the transverse attenuation, by accounting for the correct expression of the transmission coefficient in oblique incidence, which depends upon the symmetry class of the material. Third, dispersive losses were modeled here by introducing a fractional time derivative into the wave equation. Although this phenomenological approach allowed modeling the experimentally observed dispersion and attenuation for both wave polarizations, it prevents a proper identification of the underlying constitutive relation for such photopolymer materials. Towards this goal, future modeling efforts are warranted, including, for instance, the incorporation of a continuum of relaxation mechanisms (Holm *et al.*, 2013; Jazia *et al.*, 2014), which would also require measuring the viscoelastic properties over a larger frequency bandwidth.

Altogether, given that 3D printing is experiencing a wide dissemination in acoustics, the reported data will prove valuable for the computational calibration and validation of models involving structures with non-uniform properties in the MHz regime. As a next step, we will incorporate more complex mechanisms into the 3D printing process, by tailoring the spatial arrangement of the two elementary constituents [e.g., multi-material periodic media (Zhang *et al.*, 2021)] to achieve specific acoustic behaviors and to disentangle the relative contributions of material and structural properties on the measured ultrasound characteristics.

ACKNOWLEDGMENTS

This work was partially supported by the “Bonus Qualité Recherche” for young researchers (Faculté des Sciences et Technologie, Université Paris-Est Créteil, France).

APPENDIX A: ULTRASOUND CHARACTERISTICS

Table I provides the detailed values of both the measured ultrasound characteristics (at the central frequency ω_c) and the optimal model parameters $\hat{\theta}_M$ recovered using

Szabo's model. Altogether, the reported values could serve as a basis for researchers involved in the computational calibration and validation of viscoelastic models in the MHz regime.

¹See supplementary material at <https://www.scitation.org/doi/suppl/10.1121/10.0014180> for the detailed calculations that allow retrieving the total transmission coefficient in oblique incidence, as well as for the demonstration of the transverse phase velocity expression.

- Aghaei, A., Bochud, N., Rosi, G., Grossman, Q., Ruffoni, D., and Naili, S. (2022). “Ultrasound characterization of bioinspired functionally graded soft-to-hard composites: Experiment and modeling,” *J. Acoust. Soc. Am.* **151**(3), 1490–1501.
- Aliabouzar, M., Zhang, G. L., and Sarkar, K. (2018). “Acoustic and mechanical characterization of 3D-printed scaffolds for tissue engineering applications,” *Biomed. Mater.* **13**(5), 055013.
- Bakarić, M., Miloro, P., Javaherian, A., Cox, B. T., Treeby, B. E., and Brown, M. D. (2021). “Measurement of the ultrasound attenuation and dispersion in 3D-printed photopolymer materials from 1 to 3.5 MHz,” *J. Acoust. Soc. Am.* **150**(4), 2798–2805.
- BIPM, IEC, IFCC, ILAC, ISO, IUPAC, IUPAP, and OIML (2008). “Evaluation of measurement data—Guide to the expression of uncertainty in measurement,” Joint Committee for Guides in Metrology, JCGM 100(2008), 1–116.
- Chu, Y. C., and Rokhlin, S. I. (1994). “Comparative analysis of through-transmission ultrasonic bulk wave methods for phase velocity measurements in anisotropic materials,” *J. Acoust. Soc. Am.* **95**(6), 3204–3212.
- Cloonan, A. J., Shahmirzadi, D., Li, R. X., Doyle, B. J., Konofagou, E. E., and McGloughlin, T. M. (2014). “3D-printed tissue-mimicking phantoms for medical imaging and computational validation applications,” *3D Print. Addit. Manuf.* **1**(1), 14–23.
- Farinas, M. D., Álvarez-Arenas, T., Cummins, G., Desmulliez, M. P. Y., Seetohul, V., and Cochran, S. (2016). “Assessment of the ultrasonic properties of additive manufactured materials for passive components of piezoelectric transducers,” in *IEEE Int. Ultrason. Symp.*, pp. 1–4.
- Ferri, M., Bravo, J. M., Redondo, J., Jiménez-Gambín, S., Jiménez, N., Camarena, F., and Sánchez-Pérez, J. V. (2019). “On the evaluation of the suitability of the materials used to 3D print holographic acoustic lenses to correct transcranial focused ultrasound aberrations,” *Polymers* **11**(9), 1521.
- Fielder, M., and Nair, A. K. (2022). “Effects of scattering on ultrasound wave transmission through bioinspired scaffolds,” *J. Mech. Behav. Biomed. Mater.* **126**, 105065.
- He, P., and Zheng, J. (2001). “Acoustic dispersion and attenuation measurement using both transmitted and reflected pulses,” *Ultrasonics* **39**(1), 27–32.
- Holm, S., Näsholm, S. P., Prieur, F., and Sinkus, R. (2013). “Deriving fractional acoustic wave equations from mechanical and thermal constitutive equations,” *Comput. Math. Appl.* **66**(5), 621–629.
- Honarvar, F., and Varvani-Farahani, A. (2020). “A review of ultrasonic testing applications in additive manufacturing: Defect evaluation, material characterization, and process control,” *Ultrasonics* **108**, 106227.
- Jacquet, J.-R., Levassort, F., Ossant, F., and Grégoire, J.-M. (2015). “3D printed phantom for high frequency ultrasound imaging,” in *IEEE Int. Ultrason. Symp.*, pp. 1–4.
- Jacquet, J.-R., Ossant, F., Levassort, F., and Grégoire, J.-M. (2018). “3D-printed phantom fabricated by photopolymer jetting technology for high-frequency ultrasound imaging,” *IEEE Trans. Ultrason. Ferroelect. Freq. Contr.* **65**(6), 1048–1055.
- Jäger, A., Johannesmann, S., Claes, L., Webersen, M., Henning, B., and Kupnik, M. (2017). “Evaluating the influence of 3D-printing parameters on acoustic material properties,” in *IEEE Int. Ultrason. Symp.*, pp. 1–4.
- Jazia, A. B., Lombard, B., and Bellis, C. (2014). “Wave propagation in a fractional viscoelastic andrade medium: Diffusive approximation and numerical modeling,” *Wave Motion* **51**(6), 994–1010.
- Kelly, J. F., McGough, R. J., and Meerschaert, M. M. (2008). “Analytical time-domain Green's functions for power-law media,” *J. Acoust. Soc. Am.* **124**(5), 2861–2872.
- Kruisová, A., Seiner, H., Sedláček, P., Landa, M., Román-Manso, B., Miranzo, P., and Belmonte, M. (2016). “Finite elements modeling of

- mechanical and acoustic properties of a ceramic metamaterial assembled by robocasting," *Appl. Mech. Mater.* **821**, 364–371.
- Kruisová, A., Ševčík, M., Seiner, H., Sedlák, P., Román-Manso, B., Miranzo, P., Belmonte, M., and Landa, M. (2018). "Ultrasonic bandgaps in 3D-printed periodic ceramic microlattices," *Ultrasonics* **82**, 91–100.
- Kvålseth, T. O. (1985). "Cautionary note about R^2 ," *Am. Stat.* **39**(4), 279–285.
- Livingston, R., Dayal, V., and Barnard, D. (2015). "Characterization of 3D rapid prototyped polymeric material by ultrasonic methods," *AIP Conf. Proc.* **1650**, 807–816.
- Loving, J., Fielder, M., and Nair, A. K. (2018). "A numerical approach to predict fracture in bio-inspired composites using ultrasonic waves," *J. Nondestruct. Eval.* **37**(3), 1–13.
- Marczak, W. (1997). "Water as a standard in the measurements of speed of sound in liquids," *J. Acoust. Soc. Am.* **102**(5), 2776–2779.
- Miniaci, M., Krushynska, A., Gliozzi, A. S., Kherraz, N., Bosia, F., and Pugno, N. M. (2018). "Design and fabrication of bioinspired hierarchical dissipative elastic metamaterials," *Phys. Rev. Appl.* **10**(2), 024012.
- Mirzaali, M. J., Cruz Saldívar, M., Herranz de la Nava, A., Gunashekar, D., Nouri-Goushki, M., Doubrovski, E. L., and Zadpoor, A. A. (2020). "Multi-material 3D printing of functionally graded hierarchical soft-hard composites," *Adv. Eng. Mater.* **22**(7), 1901142.
- Nachman, A. I., Smith, J. F. III, and Waag, R. C. (1990). "An equation for acoustic propagation in inhomogeneous media with relaxation losses," *J. Acoust. Soc. Am.* **88**(3), 1584–1595.
- Naify, C. J., Matlack, K. H., and Haberman, M. R. (2022). "Introduction to the special issue on additive manufacturing and acoustics," *J. Acoust. Soc. Am.* **151**(1), 387–389.
- Näsholm, S. P., and Holm, S. (2011). "Linking multiple relaxation, power-law attenuation, and fractional wave equations," *J. Acoust. Soc. Am.* **130**(5), 3038–3045.
- Nelder, J. A., and Mead, R. (1965). "A simplex method for function minimization," *Comput. J.* **7**(4), 308–313.
- Niemi, J., Aitomäki, Y., and Löfqvist, T. (2005). "Ultrasonic measurements and modelling of attenuation and phase velocity in pulp suspensions," *IEEE Int. Ultrason. Symp.* **2**, 775–779.
- O'Donnell, M., Jaynes, E., and Miller, J. (1981). "Kramers–Kronig relationship between ultrasonic attenuation and phase velocity," *J. Acoust. Soc. Am.* **69**(3), 696–701.
- Papadopoulos, C. E., and Yeung, H. (2001). "Uncertainty estimation and Monte Carlo simulation method," *Flow. Meas. Instrum.* **12**(4), 291–298.
- Pearson, L. H., and Murri, W. J. (1987). "Measurement of ultrasonic wave-speeds in off-axis directions of composite materials," in *Review of Progress in Quantitative Nondestructive Evaluation* (Springer, Boston, MA), pp. 1093–1101.
- Rokhlin, S. I., and Wang, W. (1992). "Double through-transmission bulk wave method for ultrasonic phase velocity measurement and determination of elastic constants of composite materials," *J. Acoust. Soc. Am.* **91**(6), 3303–3312.
- Royer, D., and Dieulesaint, E. (1999). *Elastic Waves in Solids I: Free and Guided Propagation* (Springer Science & Business Media, New York).
- Szabo, T. L., and Wu, J. (2000). "A model for longitudinal and shear wave propagation in viscoelastic media," *J. Acoust. Soc. Am.* **107**(5), 2437–2446.
- Wu, J. (1996). "Determination of velocity and attenuation of shear waves using ultrasonic spectroscopy," *J. Acoust. Soc. Am.* **99**(5), 2871–2875.
- Yang, W., An, J., Chua, C. K., and Zhou, K. (2020). "Acoustic absorptions of multifunctional polymeric cellular structures based on triply periodic minimal surfaces fabricated by stereolithography," *Virtual Phys. Prototyp.* **15**(2), 242–249.
- Zhang, G., Liu, X., Li, X., Song, Y., and Zhang, S. (2019). "Measurement of shear wave attenuation coefficient using a contact pulse-echo method with consideration of partial reflection effects," *Meas. Sci. Technol.* **30**(11), 115601.
- Zhang, Y., Hsieh, M.-T., and Valdevit, L. (2021). "Mechanical performance of 3D printed interpenetrating phase composites with spinodal topologies," *Compos. Struct.* **263**, 113693.
- Zorzetto, L., Andena, L., Briatico-Vangosa, F., De Noni, L., Thomassin, J.-M., Jérôme, C., Grossman, Q., Mertens, A., Weinkamer, R., Rink, M., and Ruffoni, D. (2020). "Properties and role of interfaces in multimaterial 3D printed composites," *Sci. Rep.* **10**(1), 1–17.